Hydrodynamic modeling of perforated structures

Bernard Molin

Hydrodynamic modeling of perforated structures

B. Molin

École Centrale Marseille & Institut de Recherche sur les Phénomènes Hors Équilibre (IRPHE), 13451 Marseille cedex 20, France

A hydrodynamic model of perforated or slotted structures is proposed. It is asymptotic in the sense that the openings are supposed to be infinitely small and numerous, and the wall thickness to be nil. At variance with other work, a quadratic, not linear, law, relating the pressure differential to the traversing velocity, is assumed. As a result the hydrodynamic coefficients (added mass and damping) become amplitude dependent. The model is applied to bodies of various shapes including cylinders, plates and disks, in forced motion or submitted to incoming waves. Good agreement with experimental data is generally observed.

1. Introduction

This paper aims at reviewing and presenting in a synthetic and compact form a collection of work done by the author and his co-workers over a period of more than 20 years. It started in the late eighties with the hydrodynamic analysis of the "stabilizer" of the Roseau (reed) compliant tower. This stabilizer consisted in an open-ended square box attached to the jacket frame, with the 4 vertical sides composed of a dozen plates separated by horizontal slots (Fig. 1). The purpose of the stabilizer was to increase locally the horizontal added mass, in order to properly "tune" the tower with regard to the wave frequencies. Forced motion model tests with the stabilizer deeply submerged below the free surface revealed that the added mass was highly dependent on the amplitude of motion, and that it was accompanied by a strong damping.

E-mail address: bernard.molin@centrale-marseille.fr.

Another perforated or "ventilated" structure which turned out to yield a strong dependence of the added mass upon the amplitude of motion is the tubular frame shown in Fig. 2, used as a protection for subsea modules on the seabed.

Fig. 3, taken from [2], shows the measured added masses of five different such ventilated frames, divided by the solid added masses, as a function of the parameter $A(1-\tau)/(2D\tau^2)$, where A is the motion amplitude, D the short side of the frames and τ (r in the figure) the porosity or open-area ratio. It can be seen that, when plotted vs. this parameter, the five experimental curves more or less coalesce into one. It can also be noticed that, at low values of the abscissa, the added mass ratio is nearly nil.

Obviously the sensitivity of the added mass to the amplitude of motion must be related to viscous effects, that is flow separation through the slots of the stabilizer and through the openings of the tubular frame. In the theoretical model proposed here, separation is always be assumed, no matter how small the amplitude of

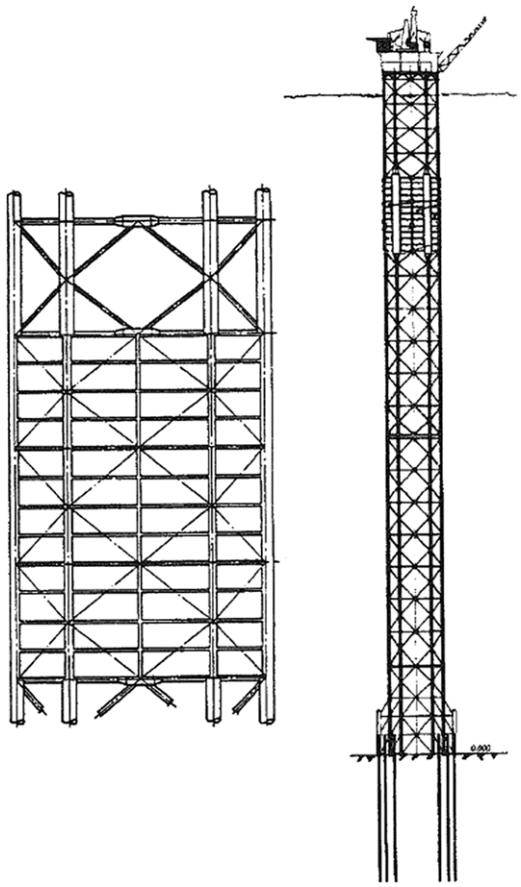

Fig. 1. The Roseau tower and its stabilizer.

Fig. 2. Example of ventilated structure, a protection cover for subsea modules [1].

motion or the size and shape of the openings. Moreover we go to the limit when the slots or openings are infinitely numerous and small, so that the only relevant geometric parameter is the open-area ratio or porosity. It must be emphasized that this is porosity defined in a superficial, not volumetric, sense.

To summarize the assumptions of our theoretical model are:

(i) negligible thickness
(ii) flow separation through the openings or slots, resulting in a quadratic discharge law
(iii) openings infinitely small and numerous.

In Section 2 we show that, as a consequence of assumption (iii), local inertia effects are negligible, that is the pressure differential only relates to the averaged traversing velocity squared, no matter

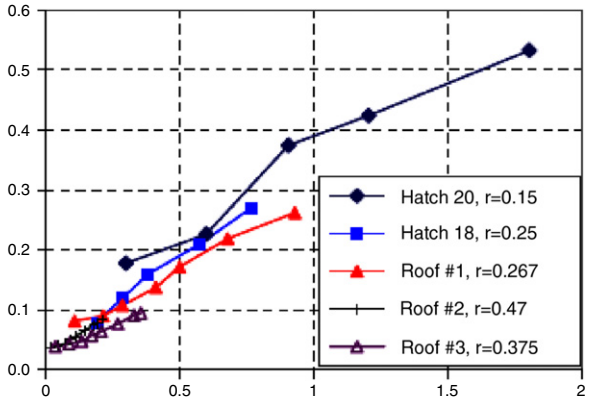

Fig. 3. Added mass ratio (ventilated/solid) vs. $A(1-\tau)/(2D\tau^2)$ for 5 ventilated structures [2].

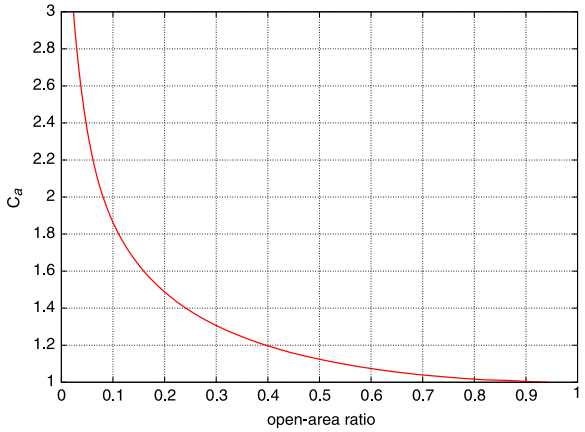

Fig. 4. Added mass coefficient vs. open-area ratio.

whether the flow and/or structure is accelerated or not. However this does not mean that the inertia loads on the global body are nil, due to phase differences between the local flow and the outer flow. In Section 3 our theoretical model is compared with other works on porous or perforated structures. Then different cases of application are presented: two- and three-dimensional cylinders (Sections 4 and 5), wave absorbers consisting in perforated plates (Section 6), plates and disks (Section 7) and water entry of perforated wedges (Section 8).

2. Theoretical model

For the sake of simplicity we consider the two-dimensional case of a channel flow through a slit or diaphragm. Be d the width of the channel and $d-2b$ the width of the diaphragm, meaning a porosity $\tau = (d-2b)/d = 1-2b/d$. From [3], the added mass of the obstruction is $M_a = C_a(\tau)\rho\pi b^2$ with

$$C_a(\tau) = \frac{8}{(1-\tau)^2\pi^2} \ln\left[\frac{1}{2}\tan\frac{\pi\tau}{4} + \frac{1}{2}\cot\frac{\pi\tau}{4}\right]. \tag{1}$$

The added mass coefficient C_m is plotted in Fig. 4 as a function of the open-area ratio τ.

Now consider a channel of width D with a series of N identical slots and solid parts of widths $(1-\tau)D/N$. The total added mass is

$$M_a = N \times \rho\pi \frac{(1-\tau)^2 D^2}{4N^2} C_a(\tau)$$
$$= \frac{2}{\pi}\rho\frac{D^2}{N} \ln\left[\frac{1}{2}\tan\frac{\pi\tau}{4} + \frac{1}{2}\cot\frac{\pi\tau}{4}\right] \tag{2}$$

and goes to zero as N goes no infinity, no matter the value of the open-area ratio τ.

So, according to potential flow theory, inertia loads are nil in the limiting case when the openings are infinitely small and numerous. This result also assumes that the wall thickness is zero.

Let us now consider viscous effects and loads resulting from flow separation. Again for a two-dimensional channel of width d with a diaphragm of width τd, if v is the averaged flow velocity far upstream and downstream the diaphragm, then v/τ is the averaged velocity through the diaphragm and the pressure differential acting on the solid part of width $(1-\tau)d$ is given by

$$\Delta P = \frac{1}{2\mu}\rho\frac{v|v|}{\tau^2} \tag{3}$$

or, considering an equivalent pressure differential Δp that applies all over the channel width:

$$\Delta p = \frac{1-\tau}{2\mu\tau^2}\rho v|v|. \tag{4}$$

Here μ is a discharge coefficient of order one. Typically $\mu \simeq 0.3-0.4$ for a perforated plate of porosity less than 50% (see the following section).

When the body is moving with respect to the fluid, the relationship (4) is generalized in

$$\Delta p = \frac{1-\tau}{2\mu\tau^2}\rho v_r|v_r| \tag{5}$$

with v_r the relative velocity in the normal direction:

$$v_r = (\overrightarrow{V}_{l,r} - \overrightarrow{U})\cdot\overrightarrow{n}. \tag{6}$$

$\overrightarrow{V}_l$ the fluid velocity on the left-hand side, $\overrightarrow{V}_r$ the fluid velocity on the right-hand side, $\overrightarrow{U}$ the local body velocity and $\overrightarrow{n}$ the normal vector to the body surface.

Mass conservation implies:

$$\overrightarrow{V}_l\cdot\overrightarrow{n} = \overrightarrow{V}_r\cdot\overrightarrow{n}. \tag{7}$$

Since the openings are assumed to be infinitely small, the wakes will be quickly regularized and homogenized, so that potential flow theory can be applied to the outer flow. The pressure is then obtained through the Bernoulli–Lagrange equation

$$p_{l,r} = H_{l,r}(t) - \rho g z - \rho\frac{\partial\Phi_{l,r}}{\partial t} - \frac{1}{2}\rho(\nabla\Phi_{l,r})^2 \tag{8}$$

with Φ_l (resp. Φ_r) the velocity potential of the left-hand side (resp. right-hand side) and $H_{l,r}$ the Bernoulli constants.

In most cases considered here the pressure is linearized in

$$p_{l,r} = -\rho g z - \rho\frac{\partial\Phi_{l,r}}{\partial t}. \tag{9}$$

3. Connection with other works

There is a wide literature on steady flow interaction with screens, gauzes and other porous surfaces. Taylor [4] makes the distinction between wire gauzes or perforated sheets, where the pressure drop relates to the square of the flow velocity, and material with very fine pores where the relationship becomes linear. A review is given by Laws and Livesey [5] for screens of low solidity ratios.

A wealth of information, relative to barriers distributed over channel flows, is to be found in [6] (chapter 8). Various formulas are given for the resistance coefficient such as

$$K = \frac{\Delta p}{1/2\rho v^2} = \frac{[0.707(1-\tau)^{3/8}+1-\tau]^2}{\tau^2} \tag{10}$$

for perforated sheets with sharp-edged orifices, or

$$K = 1.3(1-\tau) + \left(\frac{1}{\tau}-1\right)^2 \tag{11}$$

for screens made of metal wires, or

$$K = 1.28\frac{1-\tau}{\tau^2} \tag{12}$$

for two-plane screens made from bars of circular cross section.

Other formulas, similar but not identical, are gathered in [7] (chapter 10). For instance, in the case of single-plane screens with round rods at open-area ratios less than 80%, Blevins gives

$$K = \beta\frac{1-\tau^2}{\tau^2} \tag{13}$$

with $\beta = 0.52$ for Reynolds numbers larger than 400.

For slat screens, Tait et al. [8] apply

$$K = \left(\frac{1}{C_c\tau}-1\right)^2 \quad \text{with } C_c = 0.405\mathrm{e}^{-\pi(1-\tau)} + 0.595. \tag{14}$$

Blevins [7] also gives information on the effect of inclination of the flow, where it appears that the $\cos^2\theta$ law implied by Eq. (6) is applicable.

All these formulations agree on the fact that the resistance is nil when $\tau = 1$, and that is behaves as τ^{-2} when $\tau \to 0$. Hence it may always be written that

$$K = \frac{1-\tau}{\mu\tau^2} \tag{15}$$

where it is understood that μ depends on the open-area ratio, geometry of the openings, and Reynolds number, and that it must be determined on a case by case basis.

All these formulas are based on experiments in steady flow condition. Whether they remain applicable in unsteady flow is a matter of Keulegan–Carpenter number based on the amplitude of the water particle motion and on the size of the obstructions. Under our assumption of infinitely numerous openings of infinitely small size, this Keulegan–Carpenter number is infinite, meaning that the steady flow formulas also apply in unsteady flow conditions.

Another extensive literature concerns wave interaction with porous media. A review is given in [9]. In these works, the structure is assumed to be composed of a porous medium of some width, with the flow through it governed by Darcy's law. This means a linear relationship between pressure drop and traversing velocity. Following Chwang [10], many authors have used this model to tackle wave interaction with perforated bodies. For Darcy's law to be applicable the openings must be very minute as pointed out by Taylor [4]. Therefore this model is not applicable to the problems that we are dealing with here, where the openings are large and sharp enough for the flow to separate and frictional forces to be negligible as compared to pressure forces.

As quoted by Chwang and Chan [9], there is also some abundant literature dealing with unsteady flow through apertures, within potential flow theory. This means that flow separation is not accounted for. There are relatively few works dealing with unsteady separated wave flows. A review can be found in [11, chapter 6]. Most applications presented there concern wave interaction with slotted barriers and assume long wave theory, with constant horizontal velocity over the depth. The model that we present in Section 6 is not restricted to shallow water conditions.

4. A model case: the two-dimensional circular cylinder

4.1. Forced harmonic motion

We consider a perforated two-dimensional cylinder undergoing forced motion in the x direction. The fluid domain is unbounded and at rest at infinity. The motion amplitude is assumed to be

small as compared to the cylinder radius a and the equations are linearized.

The fluid domain can be decomposed into an inner domain (inside the cylinder) and an outer domain. In both domains the velocity potential can be expressed as

$$\Phi_i(R,\theta,t) = \sum_{m=1}^{\infty} A_m(t) a \left(\frac{R}{a}\right)^m \cos m\theta \quad R \le a \tag{16}$$

$$\Phi_e(R,\theta,t) = \sum_{m=1}^{\infty} B_m(t) a \left(\frac{a}{R}\right)^m \cos m\theta \quad R \ge a \tag{17}$$

with $B_m = -A_m$ so that $\partial\Phi_i/\partial R = \partial\Phi_e/\partial R$ at $R = a$.

Making use of the linearization $\cos\theta|\cos\theta| \simeq 8\cos\theta/(3\pi)$ only the $m = 1$ terms of Φ_i et Φ_e need to be retained.

The discharge equation takes the form

$$\dot{A}_1(t) = \frac{\partial A_1}{\partial t} = -\frac{2(1-\tau)}{3\pi\mu\tau^2 a}(A_1(t) - U(t))|A_1(t) - U(t)| \tag{18}$$

with $U(t)$ the cylinder velocity. This equation can be integrated in time for given $U(t)$.

In the case of a sinusoidal motion, an analytical solution can be obtained. Writing

$$U(t) = \Re\{A\omega e^{-i\omega t}\} \tag{19}$$

$$A_1(t) = \Re\{A\omega(1+b)e^{-i\omega t}\} \tag{20}$$

with A the motion amplitude and ω the frequency, and applying again the linearization

$$\Re\{f e^{-i\omega t}\}|\Re\{f e^{-i\omega t}\}| \simeq \frac{8}{3\pi}\|f\|\Re\{f e^{-i\omega t}\} \tag{21}$$

where $\|\ \|$ means the modulus of the complex number, one gets the equation

$$b\|b\| = iC(1+b) \tag{22}$$

which has the solution

$$b = \frac{\sqrt{C^2+4}-C}{2}\left(-C + i\sqrt{C\frac{\sqrt{C^2+4}-C}{2}}\right) \tag{23}$$

where

$$C = \left(\frac{3\pi}{4}\right)^2 \frac{\mu\tau^2}{1-\tau}\frac{a}{A}. \tag{24}$$

The hydrodynamic force writes

$$F_x = \Re\{i\rho\pi a^2 A\omega^2(C_a + iC_b)e^{-i\omega t}\} \tag{25}$$

with the added mass and damping coefficients

$$C_a = 2 - C(\sqrt{C^2+4} - C) \tag{26}$$

$$C_b = \sqrt{\frac{C}{2}}(\sqrt{C^2+4} - C)^{3/2} \tag{27}$$

shown in Fig. 5 as a function of the parameter $\widetilde{K_C} = (1-\tau)A/(2\mu\tau^2 a)$, which is a Keulegan–Carpenter number combined with the porosity parameter: this means that it is equivalent to increase the motion amplitude or to decrease the open-area ratio.

At zero motion amplitude, both the added mass and damping coefficients are nil: it is as though the cylinder does not exist. As the amplitude increases from zero, the added mass coefficient steadily increases to its asymptotic value of 2, which corresponds to the case of a solid cylinder full of water. In the low amplitude range the damping coefficient dominates the added mass one, until the two curves cross each other. This corresponds to the maximum

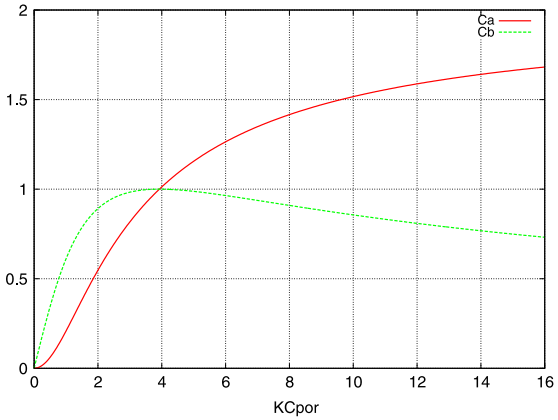

Fig. 5. Two-dimensional porous cylinder. Added mass and damping coefficients vs. $\widetilde{K_C}$.

value of the damping coefficient, which is equal to one, or half the solid case added mass coefficient. This feature has been observed for all geometries, in two and three dimensions (in infinite fluid, i.e. without a free surface): the maximum value of the damping coefficient is always half the solid added mass coefficient and the two curves always intersect at that point.

The two-dimensional circular cylinder seems to be the only geometry that admits an analytical solution. It was first given by Molin [12]. In the other considered cases, the main numerical difficulty resides with the nonlinearity of the discharge equation. Two methods have been used to overcome this problem: solve in the time domain, or proceed through iterations so that a linear problem be solved at each iteration. As an illustration we show the obtained results when Eq. (22) is solved iteratively through the scheme

$$b^{(i)} = \frac{iC}{\|b^{(i-3/2)}\| - iC} \tag{28}$$

where $(i-3/2)$ means the averaged value between the previous two iterations $(i-1)$ and $(i-2)$ (in order to introduce some relaxation in the iterative scheme).

Fig. 6 shows that the iterative scheme is most efficient at low values of the parameter $\widetilde{K_C}$. At large $\widetilde{K_C}$ values other iterative schemes can be devised (e.g. see [13]).

4.2. Nonharmonic motion

Let us consider the general case of a complex (for instance bichromatic) motion with velocity $(U(t), V(t))$ in x and y direction. We also add up a current in the x direction with velocity C. A time domain resolution method can then be employed, as follows.

In a reference frame linked to the cylinder the absolute velocity potential can be expressed as

$$\Phi_i(R,\theta,t) = \sum_{n=1}^{N} a\left(\frac{R}{a}\right)^n [A_n(t)\cos n\theta + B_n(t)\sin n\theta] \quad R \le a \tag{29}$$

$$\Phi_e(R,\theta,t) = -\sum_{n=1}^{N} a\left(\frac{a}{R}\right)^n [A_n(t)\cos n\theta + B_n(t)\sin n\theta] + C\left(R + \frac{a^2}{R}\right)\cos\theta \quad R \ge a. \tag{30}$$

The pressure being given by

$$p = H(t) - \rho\Phi_t - \frac{1}{2}\rho(\nabla\Phi)^2 + \rho\,\overrightarrow{U}_E \cdot \nabla\Phi \tag{31}$$

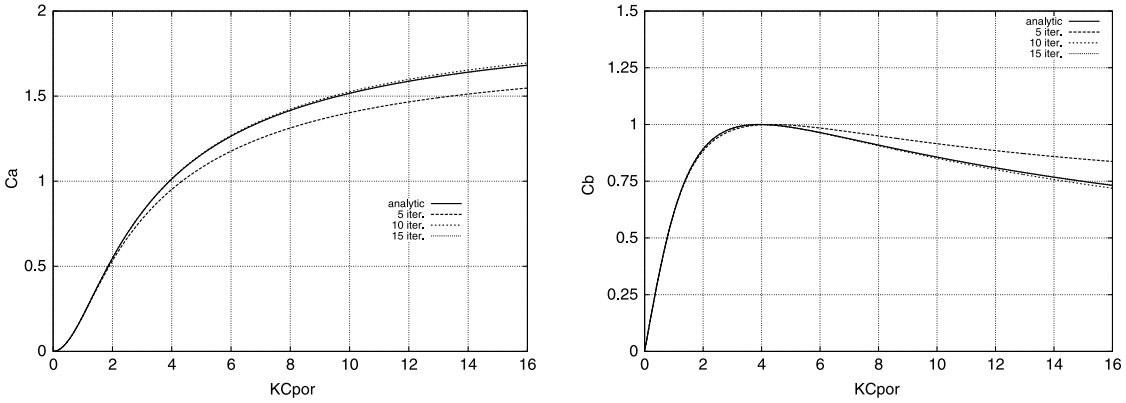

Fig. 6. Two-dimensional porous cylinder. Iterative resolution of the added mass (left) and damping (right) coefficients vs. $\widetilde{K_C}$.

with $\overrightarrow{U}_E = (U, V)$, the discharge equation can finally be put in the form [14]:

$$\sum_{n=1}^{N} \dot{A}_n \cos n\theta + \dot{B}_n \sin\theta = f(\theta, t) \tag{32}$$

with

$$\begin{aligned} f(\theta,t) = {} & \frac{1}{a}[(C-U)\sin\theta + V\cos\theta] \\ & \times \left[C\sin\theta - \sum_{n=1}^{N} n(A_n \sin n\theta - B_n \cos n\theta) \right] \\ & + \frac{K(t)}{2\rho a} - \frac{1-\tau}{4\mu\tau^2 a} \left[\sum_{n=1}^{N} n(A_n \cos n\theta + B_n \sin n\theta) \right. \\ & \left. - U\cos\theta - V\sin\theta \right] \\ & \times \left| \sum_{n=1}^{N} n(A_n \cos n\theta + B_n \sin n\theta) \right. \\ & \left. - U\cos\theta - V\sin\theta \right|. \end{aligned} \tag{33}$$

The coefficients $A_n(t), B_n(t)$ therefore obey the evolution equations

$$\dot{A}_n = \frac{1}{\pi} \int_0^{2\pi} f(\theta, t) \cos n\theta \, \mathrm{d}\theta \tag{34}$$

$$\dot{B}_n = \frac{1}{\pi} \int_0^{2\pi} f(\theta, t) \sin n\theta \, \mathrm{d}\theta. \tag{35}$$

These are integrated in time, from initial values corresponding, for instance, to the solid cylinder case. At any time the hydrodynamic load is obtained as

$$F_x = -2\pi\rho a[a\dot{A}_1 + (C-U)A_2 - VB_2] \tag{36}$$

$$F_y = -2\pi\rho a[a\dot{B}_1 + (C-U)B_2 + VA_2]. \tag{37}$$

In [15,16] application is made to a bichromatic forced motion, representative, for instance, of combined wave frequency response and slow-drift motion of a moored or compliant structure. It turns out that the hydrodynamic coefficients of each motion component can be very different from the values they take in single harmonic motion. This means, for instance, that the low frequency motion can be heavily damped in still water but not in waves; or the other way around [16].

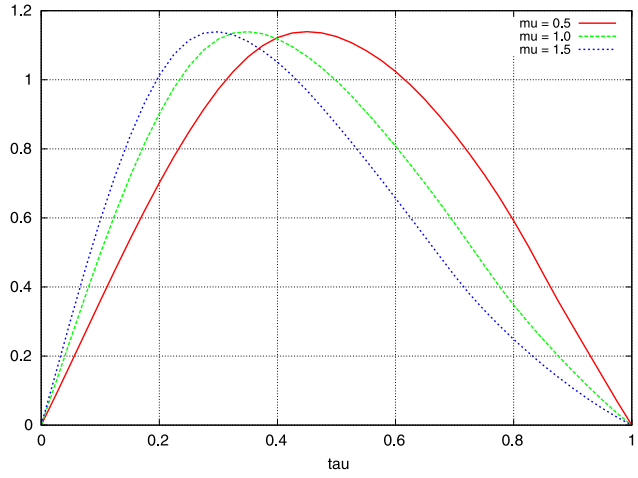

Fig. 7. Two-dimensional porous cylinder. Drag coefficient in current vs. open-area ratio τ.

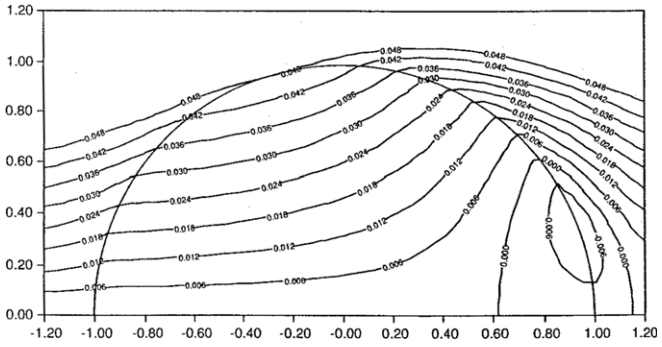

Fig. 8. Two-dimensional porous cylinder in current. Calculated streamlines in the case $\tau = 0.5$, $\mu = 1$.

Fig. 7 shows the drag coefficients derived from the time domain simulations, in current only, as a function of the porosity ratio τ, for different values of the discharge coefficient μ. Due to the potential flow model assumed the drag coefficient is zero when the cylinder is solid ($\tau = 0$), so our results are unphysical at low porosities. It is noteworthy that the drag coefficient peaks at about 1.15, a value very close to the drag coefficient for a solid cylinder in subcritical flow. Fig. 8 shows the calculated streamlines when $\tau = 0.5$ and $\mu = 1$. Molin [17] presents a similar investigation for the case of shrouded cylinders, with qualitative agreement with available results from the literature.

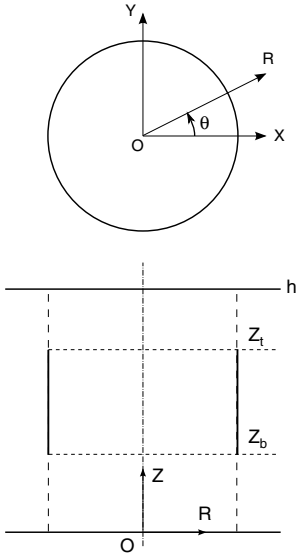

Fig. 9. Three-dimensional porous cylinder. Geometry.

5. Three-dimensional circular cylinder

This case was also considered by Molin [12]. Further information can be found in [18], where the problem is solved in the frequency domain, or [15] where a time domain resolution method is used.

The problem is formulated in cylindrical coordinates (R, θ, z) with the vertical cylinder extending from z_b to z_t. The fluid domain is bounded, some distance away from the cylinder edges, by two planes $z = 0$ and $z = h$ where a no-flow condition is assumed. The cylinder is located midway in between the two planes (see Fig. 9).

The cylinder being again given a forced motion with velocity $U(t)$ in the x-direction, the velocity potential can be expressed under the form

$$\Phi_i(R, z, \theta, t) = \left\{ A_0(t)\frac{R}{a} + \sum_{n=1}^{\infty} A_n(t) \cos k_n z \frac{I_1(k_n R)}{I_1'(k_n a)} \right\} \cos\theta \quad R \le a \tag{38}$$

$$\Phi_e(R, z, \theta, t) = \left\{ -A_0(t)\frac{a}{R} + \sum_{n=1}^{\infty} A_n(t) \cos k_n z \frac{K_1(k_n R)}{K_1'(k_n a)} \right\} \cos\theta \quad R \ge a \tag{39}$$

with $k_n = 2n\pi/h$ and I_1, K_1 the modified Bessel functions of order 1.

Here we briefly present the iterative frequency domain resolution. $U(t) = A\omega \cos\omega t$ being again the imposed velocity, we look for Φ_i and Φ_e under the form $\Re\{\varphi(R, \theta, z) \exp(-\mathrm{i}\,\omega t)\}$ and introduce the new unknowns a_n such that:

$$\varphi_i - \varphi_{e|_{R=a}} = \sum_{n=0}^{N} a_n \cos k_n z \cos\theta \tag{40}$$

$$\varphi_{R|_{R=a}} = \sum_{n=0}^{N} \alpha_n a_n \cos k_n z \cos\theta \tag{41}$$

with $\alpha_0 = (2a)^{-1}$ and $\alpha_n = k_n[\frac{I_1(k_n a)}{I_1'(k_n a)} - \frac{K_1(k_n a)}{K_1'(k_n a)}]^{-1}$.

The following equations are then derived

$$\sum_{n=0}^{N} a_n \cos k_n z = 0 \qquad 0 \le z \le z_b \quad z_t \le z \le h \tag{42}$$

$$\left(\sum_{n=0}^{N} \alpha_n a_n \cos k_n z - A\omega \right) \left\| \sum_{n=0}^{N} \alpha_n a_n \cos k_n z - A\omega \right\| = \mathrm{i}\, C' \sum_{n=0}^{N} a_n \cos k_n z \qquad z_b \le z \le z_t \tag{43}$$

with $C' = 2(3\pi/8)^2 \mu \tau^2/(1-\tau)$.

We define the suite $a_n^{(i)}$ and the complex z function

$$f^{(i)}(z) = -\frac{\mathrm{i}}{C'} \left\| \sum_{n=0}^{N} \alpha_n a_n^{(i)} \cos k_n z - A\omega \right\|. \tag{44}$$

Eqs. (42) and (43) now take the form

$$\sum_{n=0}^{N} a_n^{(i)} \cos k_n z = 0 \qquad 0 \le z \le z_b \quad z_t \le z \le h \tag{45}$$

$$\sum_{n=0}^{N} [1 - \alpha_n f^{(i-3/2)}(z)] a_n^{(i)} \cos k_n z = -A\omega f^{(i-3/2)}(z) \qquad z_b \le z \le z_t. \tag{46}$$

Multiplying the first equation by $\cos k_m z$, the second one by $\cos k_m z/[1 - \alpha_m f^{(i-3/2)}(z)]$, integrating in z over their respective domains of validity and adding up for $m = 0, 1, \ldots, N$ gives a linear system which is solved with a standard Gauss method. This process is repeated (and the matrix rebuilt at each iteration) until convergence is reached.

Molin and Legras [18] report an experimental campaign, carried out in the offshore tank of ENSM Nantes (now ECN, École Centrale Nantes), on stabilizers of octagonal shapes, of height 1 m and equivalent radius 0.5 m, located at mid-depth of the 3 m deep basin. This meant, roughly, a scale of 1:60 with respect to the full scale stabilizer. As can be seen in the photographs of Fig. 10, both slotted and perforated models were tested, with two different open-area ratios (10% and 24% in the perforated case, 10% and 20% in the slotted one). The wall thickness was 1 mm and the opening diameter 2 mm (in the perforated case).

Fig. 11, taken from [18], shows measured and calculated values of the added mass (left) and damping (right) coefficients, in the 10% perforated case. The motion amplitudes on the horizontal axis are full scale values, to be referred to an equivalent diameter of 60 m. So 5 m means a Keulegan–Carpenter number $KC = 2\pi A/D$ around 0.5. There is some scatter in the experimental results, but it is clear that the experimental added mass does go to zero or nearly zero as the motion amplitude decreases. The agreement between experimental and numerical added mass coefficients is rather good all over the range of motion amplitude. As for the damping coefficient, the agreement slightly deteriorates as the motion amplitude increases. This has been identified to be related to flow separation at the lower and upper edges of the stabilizer, an effect which is not accounted for by our theoretical model. The dotted curve is simply obtained by adding up, to the calculated damping force, a viscous force in the form $F_D = -1/2\rho C_D S V|V|$, with a drag coefficient C_D equal to 5.

Very similar results were obtained in the slotted case, meaning that open-area ratios matter a lot more than the shape of the openings, as assumed in our theoretical model.

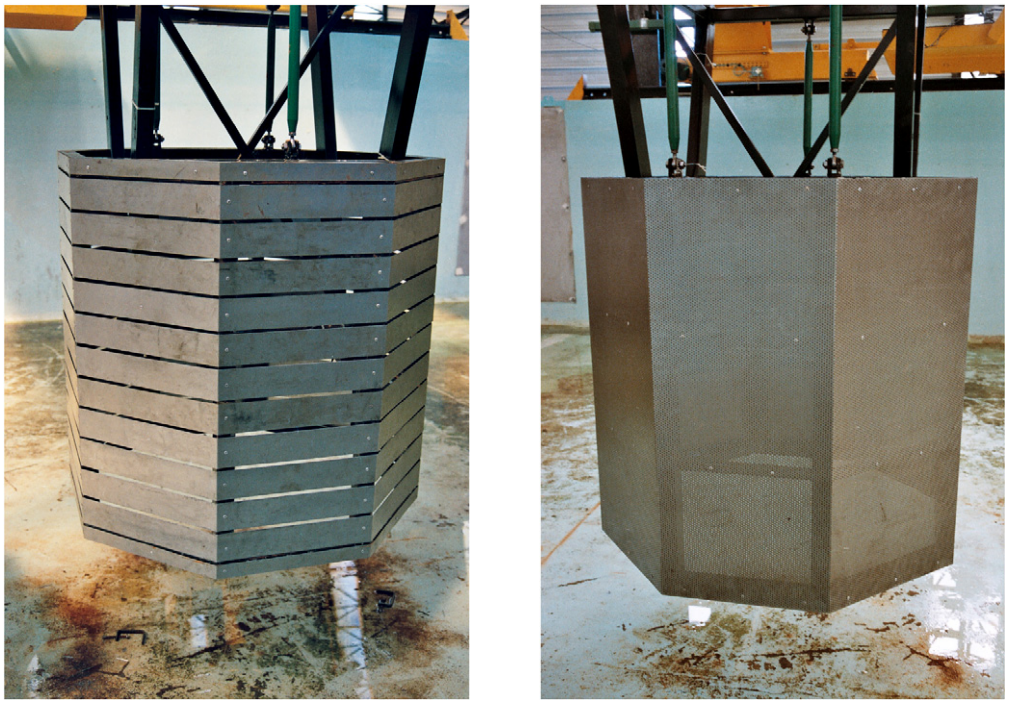

Fig. 10. Experimental octagonal stabilizers (10% and 24% porosity ratios).

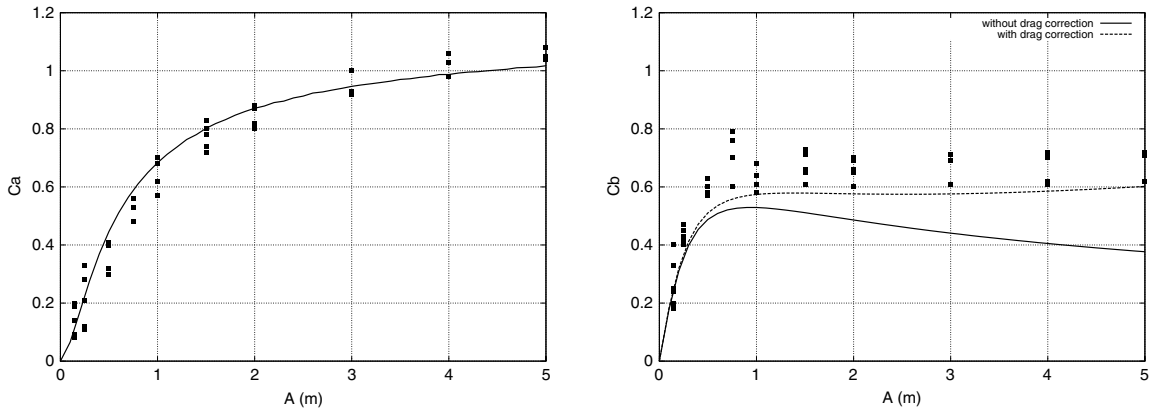

Fig. 11. Perforated stabilizer at 10% porosity. Added mass (left) and damping (right) coefficients, vs. motion amplitude, from measurements (symbols) and from calculations.

6. Regular wave interaction with perforated or slotted plates

There is an abundant literature on wave interaction with slotted barriers. A paper often quoted is due to Isaacson et al. [19]. They refer to Sollitt and Cross [20] to propose a linear discharge law linking the pressure differential and the traversing velocity. However Sollitt and Cross' formulation was devised for rubble mound breakwaters idealized as a rectangular porous medium of some length b in the wave direction. The porosity that appears in their formulation is a volumetric porosity, not an open-area ratio. As a result of using Sollitt and Cross' formulation, the barrier width b remains in Isaacson et al.'s expression. This makes little sense in the case of perforated or slotted walls of small thickness. A linear discharge law also means that there is no effect of the wave steepness.

Jamieson and Mansard [21] present an extensive experimental investigation on wave absorbers consisting in series of perforated vertical plates. Such "progressive wave absorbers" are used in some wavetanks to damp out incoming waves and minimize wave reflection, in the same purpose as parabolic beaches. The experimental results of Jamieson and Mansard [21] give evidence that the hydrodynamic performances of vertical perforated plates vary with the wave steepness.

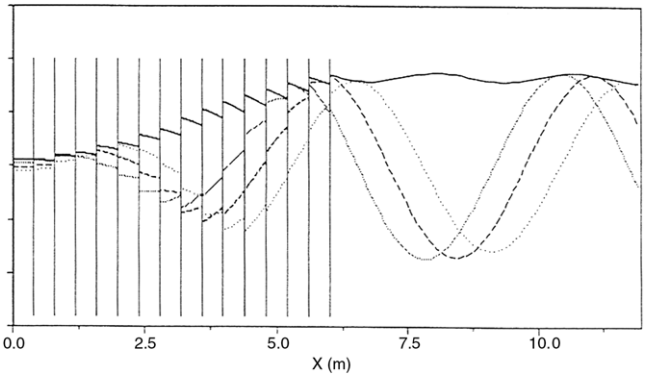

Fig. 12. Regular wave interaction with a progressive wave absorber. Free surface elevation envelope and profile at three different instants [13].

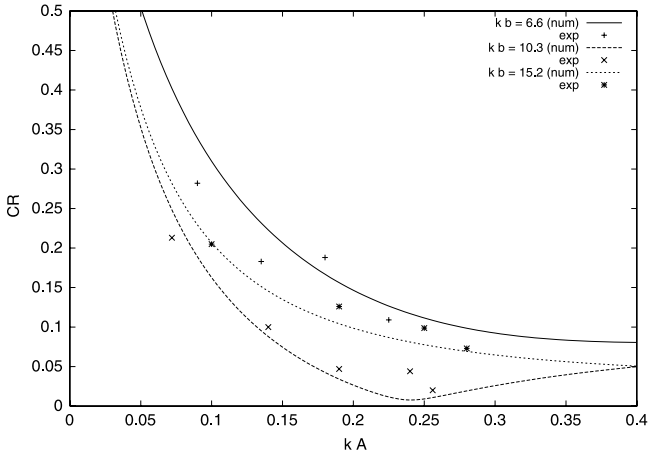

Fig. 13. Submerged horizontal plate. Measured and calculated values of the reflection coefficient vs. the wave steepness [24].

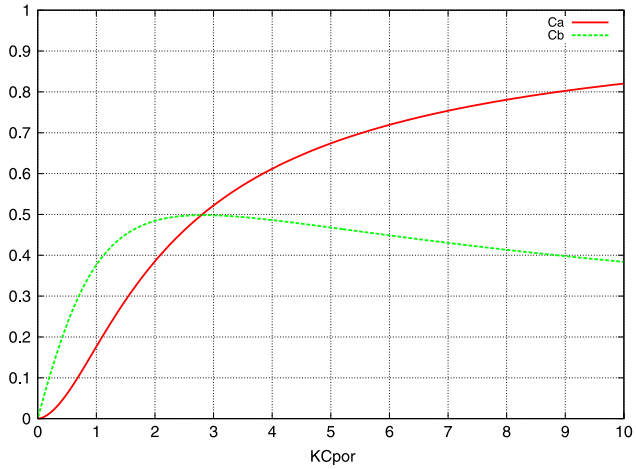

Fig. 14. Two-dimensional porous plate in unbounded fluid. Added mass and damping coefficients vs. $\widetilde{K_C}$.

Molin and Fourest [13] developed a numerical model that predicts regular wave interaction with a series of vertical perforated plates followed by a vertical wall. Because of the free surface condition it is difficult to solve the problem in the time domain and an iterative frequency domain scheme is used. The absorber consisting of N vertical plates, the fluid domain is divided in $N + 1$ rectangular sub-domains where the velocity potential is decomposed as a series of propagative and evanescent modes. Good agreement is obtained with the experimental results of [21]. Fig. 12 shows an illustrative result for the case of a 15 plate absorber, 6 m long; the waterdepth is 1 m, the wave period is 2 s, and the steepness kA is equal to 0.2.

Kimmoun [22] uses a similar method to optimize a side wall absorber consisting in 6 vertical plates of limited draft. The performances of the optimized absorber are verified through dedicated experiments in the wave flume of École Centrale Marseille (ECM). In [23] the simpler case of a single vertical plate is studied experimentally, also in the ECM flume, and numerically up to second order in the wave amplitude.

Molin and Bétous [25] treat the case of a horizontal perforated plate below the free surface. This is also solved through eigenfunction expansions and iterations. Only numerical results are shown. In [24] experimental results are given for a submerged plate at the end of the ECM flume and an efficient iterative scheme is devised. Good agreement is obtained between experimental and numerical values of the reflection coefficient which appears to be highly sensitive to the incoming wave steepness (Fig. 13).

7. Hydrodynamic coefficients for plates and disks

7.1. Two-dimensional plate in unbounded fluid

This case has some relevance for bilge keels of FPSOs or skirts of offloading buoys. For instance the N'Kossa barge, made of concrete, has slotted bilge keels [26]. The two-dimensional plate case has much similarity with the axisymmetric disk case considered in the next section (it is just a matter of moving from (x, z) to (R, z)), so the equations are not detailed. The technique used, as in the Roseau stabilizer case, is to bound the fluid domain by two distant walls and to use eigen-function expansions and iterate, or solve in the time domain.

The plate motion being $A \sin \omega t$ and the hydrodynamic force being expressed as

$$F = \rho \pi b^2 A \omega^2 [C_a \sin \omega t - C_b \cos \omega t]. \tag{47}$$

Fig. 14 shows the added mass C_a and damping C_b coefficients as a function of the "porous Keulegan–Carpenter number" here defined as $\widetilde{K_C} = (1 - \tau)A/(2\mu\tau^2 b)$ with A the amplitude of motion and b the half-width of the plate. It can be seen that the damping coefficient peaks at 0.5, that is half the solid added mass value, when the two curves intersect. As written earlier this feature has always been observed for perforated bodies in unbounded fluid.

Note that the physical validity of these results is more and more questionable as $\widetilde{K_C}$ increases from zero, as the flow separation at the plate edge is not accounted for (see the following section).

7.2. Disks

Interest for disks first rose from the heave plates used to increase the heave added mass and damping of spar platforms. These plates are solid, except for a central opening to give way to the risers. Perforating them could be beneficial in the way that it would increase the damping effect and decrease the added mass, hence the structural loads. Usually more than one plate are piled up and attached to the jacket frame of the spar. When the plates are sufficiently close there are interaction effects that should be accounted for.

In [27] the case of an infinite and periodic array of disks, in unbounded fluid, is tackled. The problem is solved in the time domain. (Time domain had been chosen because the initial purpose was to solve the heave motion of a truss spar under irregular waves, meaning several frequency components in the loading and response.)

Subsequently there had been some interest from the oil offshore industry for hydrodynamic coefficients of structures such as the protection cover shown in Fig. 2, during installation, all the way from slightly below the free surface to the seafloor. Other "ventilated" structures that create installation problems are suction anchors or mudmats. Mudmats and hatch covers are rectangular, but they were idealized as disks of equivalent area in [1] where a numerical model is presented that gives the heave added mass and damping of perforated disks under the free surface. The imposed motion is supposed to be harmonic and the problem is solved in the frequency domain, through iterations.

When the separation distance in the disk array is taken sufficiently large, and when the isolated disk is sufficiently far away from the free surface and seafloor, the same hydrodynamic coefficients should be obtained. This is shown in Fig. 15, as a function of the porous Keulegan–Carpenter here defined as $\widetilde{K_C} = (1 - \tau)A/(2\mu\tau^2 a)$ with A the motion amplitude and a the radius of the disk. There are slight differences between the two sets of results,

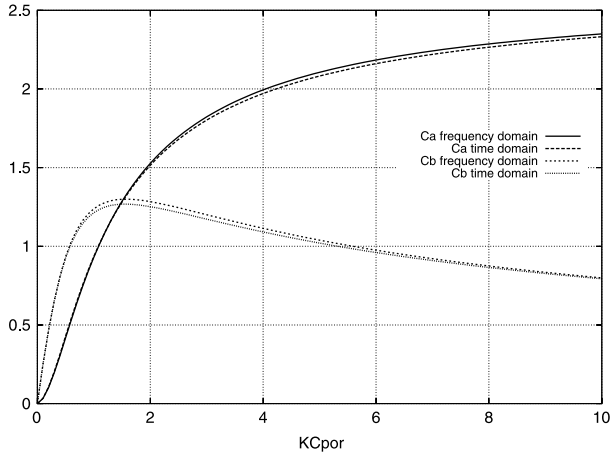

Fig. 15. Porous disk in unbounded fluid. Added mass and damping coefficients vs. $\widetilde{K_C}$.

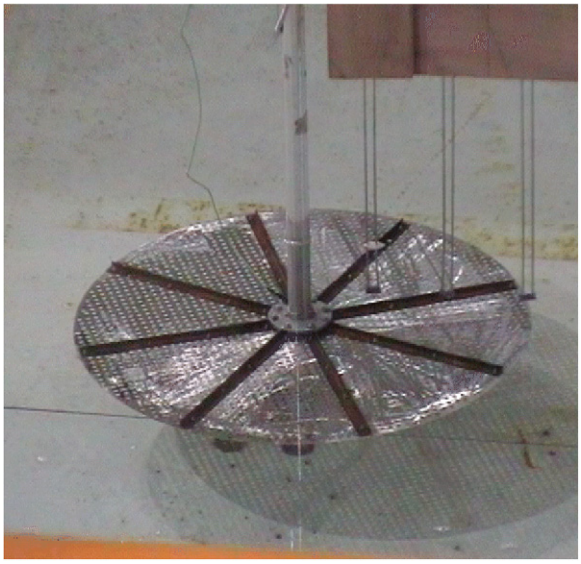

Fig. 16. Perforated disk below the free surface. Porosity 20%.

partly due to the fact that the problem is solved in the time domain in one case and in the frequency domain in the other one (such small discrepancies are also obtained for porous cylinders; see Fig. 3 in [15], for instance); taking the disks far apart in the case of the disk array, or far away from both the free surface and seafloor in the case of the isolated disk, also hinders numerical convergence and the truncation orders of the series are presumably too low (see the discussion in [1]). The added mass and damping are made nondimensional by dividing them by ρa^3 and $\rho a^3 \omega$ respectively. Hence the asymptotic value of the added mass coefficient is 8/3 and the damping coefficient peaks at 4/3 when the two curves intersect.

In [28] some experiments are reported on disks of diameters 60 cm and thickness 1 mm (with some radial stiffening to prevent deformation), at porosities 0% (solid), 10%, and 20%. The waterdepth is 50 cm and the disks are oscillated at various distances from the free surface and bottom. A photograph of the 20% porosity model is shown in Fig. 16.

Fig. 17, taken from [28], shows the measured and calculated values of the added mass and damping coefficients, vs. the amplitude of motion, with the disk at mid-depth and the oscillation period equal to 1.2 s. At this combination of period and immersion there are negligible free surface and bottom effects. There are two sets of

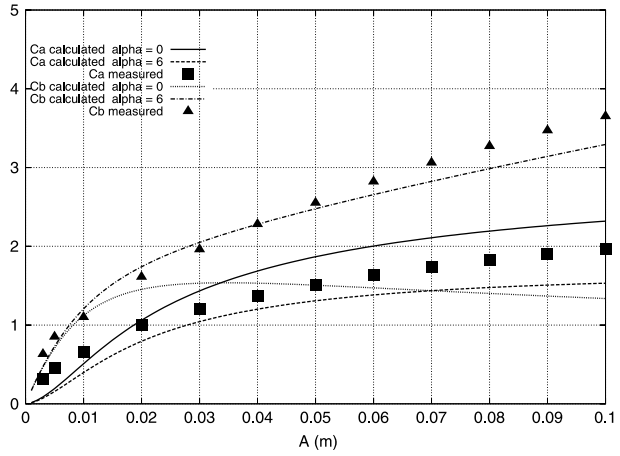

Fig. 17. Perforated disk at porosity 20%. Immersion 25 cm. Period 1.2 s. Measured and calculated added mass and damping coefficients.

numerical curves, labeled as $\alpha = 0$ and $\alpha = 6$, a non-zero value of α meaning an empirical correction to account for flow separation at the disk outer rim. Without this correction the calculated and measured values quickly diverge as the motion amplitude increases and the range of validity of our numerical model is restricted to very low values of the motion amplitude, or of the $\widetilde{K_C}$ parameter.

The viscous correction consists in adding up to the hydrodynamic load a drag term, in the form

$$F_v = -\frac{1}{2}\rho C_D \pi a^2 V_R |V_R| \tag{48}$$

with $C_D = \alpha KC^{-1/3}$ and $KC = \pi A/a$, as proposed by Sandvik et al. [2]. The $KC^{-1/3}$ dependence of the drag coefficient is based on [29]. At low KC the α value strongly depends on the diameter over thickness ratio of the disk [30]. In the case of their rather thick and edge-rounded hatch covers, [2] obtain that $\alpha = 2$ gives the best fit with the experimental results. In [28], experiments with solid disks are first reported where it is found that the α value should be taken much higher! In Fig. 17 $\alpha = 6$ provides a reasonably good fit with the experiments in the considered case. The relative velocity V_R in Eq. (48) is taken as the disk velocity minus the relative fluid velocity through the disk, averaged over the disk; this results in a modification of the added mass coefficient as well. It should be noted that when this viscous correction is applied, the hydrodynamic coefficients depend no more on the $\widetilde{K_C}$ value alone, but both on $\widetilde{K_C}$ and on KC.

Fig. 18, also extracted from [28] shows the added mass and damping coefficients when the disk is oscillated just below the free surface, at 5 cm from the still water level. At 0.8 s period the agreement between experimental and numerical values is rather good and the viscous correction, as formulated above, is unnecessary. At 1.6 s there appears quickly deviations for the added mass coefficient; as a matter of fact such deviations also appear for the solid disk where nonlinear free surface effects in the shallow region above the disk seem to quickly come into play at oscillation periods larger than 1.2 s.

8. Water entry

An operational problem related to well-head covers such as shown in Fig. 2 is their installation procedure and possible wave loads when lifted through the splash zone. It is intuitive that a perforated body will endure much lower slamming loads than the equivalent solid body, but to which extent?

In order to quantify this expected reduction the academic case of the water entry of a perforated wedge has been considered

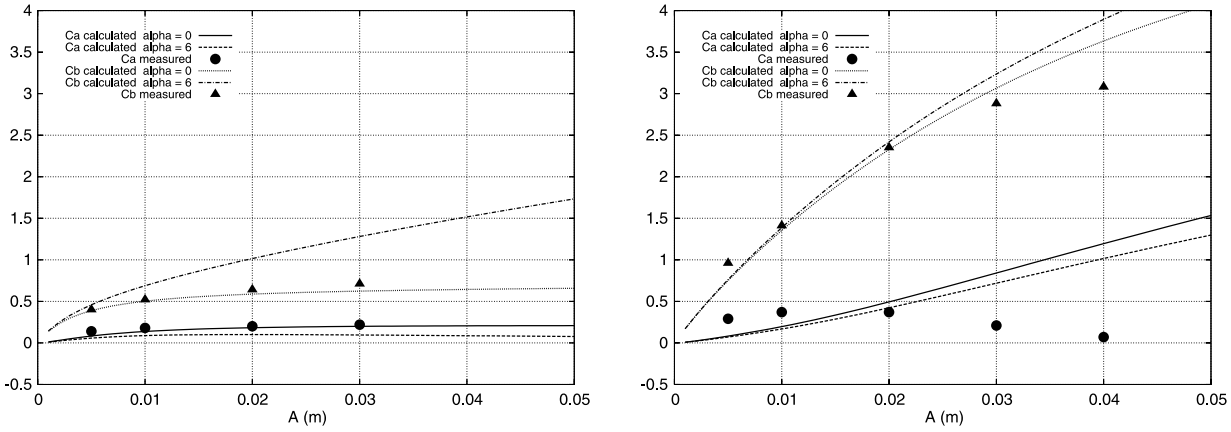

Fig. 18. Perforated disk at porosity 20%. Immersion 5 cm. Measured and calculated added mass and damping coefficients. Period 0.8 s (left) and 1.6 s (right).

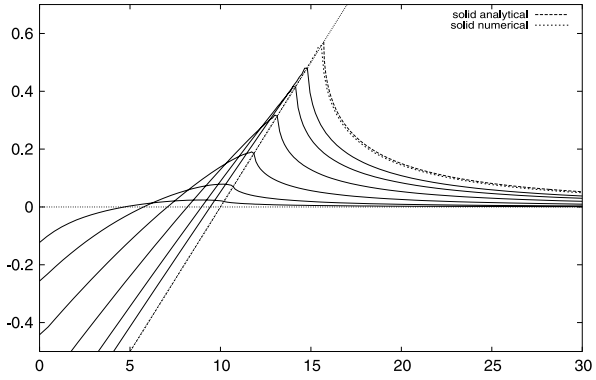

Fig. 19. Water entry of a porous wedge. $\cot\beta = 10$. Free surface elevation obtained from self-similar solution for $\alpha = 1, 4, 16, 64, 256, 1024$ and for a solid wedge.

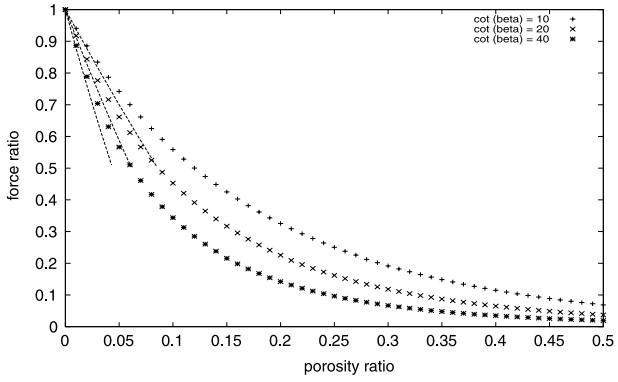

Fig. 20. Water entry of a porous wedge. Vertical force as a function of the porosity ratio τ, for different deadrise angles.

in [31]. This simple geometry permits to exhibit a self-similar solution, which is obtained through iterations.

Fig. 19, taken from [31], shows the free surface elevations obtained for a wedge of deadrise angle β such that $\cot\beta = 10$, for different values of the parameter $\alpha = (1-\tau)/(2\mu\tau^2)$ and for the solid case. These are the free surface elevations in an averaged sense: practically jets would be seen flowing upward through the wedge openings.

Fig. 20, also taken from [31], shows the reduction factor of the vertical hydrodynamic load, as a function of the porosity τ, for three different values of the deadrise angles. (Straight lines at the origin are asymptotic results for small open-area ratios). It can be observed that the reduction factor is appreciable: for instance with a porosity of 20% the load decreases by a factor 7 for the flattest wedge!

9. Final comments

We have considered several application cases which, in our opinion, give evidence that our theoretical model, described in Section 2, has some practical validity. As much as we could we have presented comparisons with experimental results, with convincing agreement except for the edge effect which, in the case of disks or hatch covers, limits the range of validity of our model to small values of the porous Keulegan–Carpenter number $\widetilde{K_C}$ (as a rule of thumb, to the upward part of the damping curve). Some results that we have presented are purely numerical however, like the drag coefficient of the two-dimensional cylinder shown in Fig. 7, or the water entry of the perforated wedge. On these cases confrontations with experimental measurements seem to be desirable.

These findings suggest that perforating parts of marine or offshore structures can be an efficient means for reducing inertia and slamming loads, and for increasing the damping of resonant responses. There are many potential applications, like bilge keels, heave plates of truss spars (e.g. see [32]), bodies that must be lifted down through the splash zone like mudmats and hatch covers [33], etc.

References

[1] Molin B, Nielsen FG. Heave added mass and damping of a perforated disk below the free surface. In: Proc. 19th int. workshop water waves & floating bodies. 2004. http://www.iwwwfb.org.

[2] Sandvik PC, Solaas F, Nielsen FG. Hydrodynamic forces on ventilated structures. In: Proc. sixteenth intern. offshore and polar eng. conf., ISOPE. vol. 4. 2006. p. 54–8.

[3] Morse PM, Ingard KU. Theoretical acoustics. New-York: McGraw-Hill; 1968.

[4] Taylor GI. Fluid flow in regions bounded by porous surfaces. Proc R Soc London Ser A 1956;234:456–75.

[5] Laws EK, Livesey JL. Flow through screens. Annu Rev Fluid Mech 1978;10: 247–66.

[6] Idelchik IE. Handbook of hydraulic resistance. Begell House; 1996.

[7] Blevins RD. Applied fluid dynamics handbook. Krieger; 1992.

[8] Tait MJ, El Damatty AA, Isyumov N, Siddique MR. Numerical flow models to simulate tuned liquid dampers (TLD) with slat screens. J Fluids Struct 2005; 20:1007–23.

[9] Chwang AT, Chan AT. Interaction between porous media and wave motion. Annu Rev Fluid Mech 1998;30:53–84.

[10] Chwang AT. A porous-wavemaker theory. J Fluid Mech 1981;132:395–406.

[11] Mei CC. The applied dynamics of ocean surface waves. Wiley-Interscience; 1983.

[12] Molin B. On the added mass and damping of porous or slotted cylinders. In: Proc. 4th int. workshop water waves & floating bodies. 1989. http://www.iwwwfb.org.

[13] Molin B, Fourest J-M. Numerical modeling of progressive wave absorbers. In: Proc. 7th int. workshop water waves & floating bodies. 1992. http://www.iwwwfb.org.

[14] Molin B. Projet DYNATOUR. Hydrodynamique du stabilisateur (deuxième partie). IFP report 38 368. 1990 [in French].

[15] Damy G, Molin B. Stabilizers for compliant towers: numerical and experimental studies. Brazil Offshore'91. 1991.

[16] Molin B. Motion damping by slotted structures. In: van den Boom HJJ, editor. Hydrodynamics: computations, model tests and reality. Developments in marine technology, vol. 10. Elsevier; 1992.
[17] Molin B. A potential flow model for the drag of shrouded cylinders. J Fluids Struct 1993;7:29–38.
[18] Molin B, Legras J-L. Hydrodynamic modeling of the Roseau tower stabilizer. In: Proc. 9th OMAE conference. 1990. p. 329–36.
[19] Isaacson M, Baldwin J, Premasiri S, Yang G. Wave interactions with double slotted barriers. Appl Ocean Res 1999;21:81–91.
[20] Sollitt CK, Cross RH. Wave transmission through permeable breakwaters. In: Proc. 13th ASCE conf. coastal eng. 1972. p. 1827–46.
[21] Jamieson WW, Mansard EPD. An efficient upright wave absorber. In: ASCE specialty conference on coastal hydrodynamics. University of Delaware; 1987. p. 1–15.
[22] Kimmoun O. Porous wave absorber. Optimization and experiments, Actes 9èmes Journées de l'Hydrodynamique. Poitiers. 2003. p. 327–40 [in French]. http://website.ec-nantes.fr/actesjh/.
[23] Kimmoun O, Molin B, Moubayed W. Second-order analysis of the interaction of a regular wave train with a vertical perforated wall. Actes 8èmes Journées de l'Hydrodynamique. Nantes; 2001. p. 85–98 [in French]. http://website.ec-nantes.fr/actesjh/.
[24] Molin B. Numerical and physical wavetanks: making them fit. Ship Technol Res 2001;48:2–22.
[25] Molin B, Bétous P. Atténuation de la houle par une dalle horizontale immergée et perforée. Actes 4èmes Journées de l'Hydrodynamique. Nantes; 1993. p. 387–400 [in French]. http://website.ec-nantes.fr/actesjh/.
[26] Valenchon C, Nagel R, Viallon JP, Belbeoc'h H, Rouillon J. The Nkossa concrete oil production barge. In: Proc. deep offshore technology conf. 1995.
[27] Molin B. On the added mass and damping of periodic arrays of fully or partially porous disks. J Fluids Struct 2001;15:275–90.
[28] Molin B, Remy F, Rippol T. Experimental study of the heave added mass and damping of solid and perforated disks close to the free surface. In: Maritime industry, ocean engineering and coastal resources. Taylor & Francis; 2008. p. 879–87.
[29] Graham JMR. The forces on sharp-edged cylinders in oscillatory flow at low Keulegan–Carpenter numbers. J Fluid Mech 1980;97:331–46.
[30] He H, Troesch AW, Perlin M. Hydrodynamics of damping plates at small *KC* numbers. In: IUTAM symposium on fluid-structure interaction in ocean engineering. Springer-Science; 2008. p. 93–104.
[31] Molin B, Korobkin AA. Water entry of a perforated wedge. In: Proc. 17th int. workshop water waves & floating bodies. 2001. http://www.iwwwfb.org.
[32] Downie MJ, Graham JMR, Hall C, Incecik A, Nygaard I. An experimental investigation of motion control devices for truss spars. Marine Struct 2000; 13:75–90.
[33] Pétrié F, Rousse B, Ricbourg C, Molin B, de Hauteclocque G. Installation of large subsea package. In: Deep oil technology conf. 2009.